

Powering Quantum Computation with Quantum Batteries

Yaniv Kurman,¹ Kieran Hymas,¹ Arkady Fedorov,² William J. Munro,³ and James Quach^{1,*}

¹Commonwealth Scientific and Industrial Research Organisation (CSIRO), Clayton, Victoria 3168, Australia

²School of Mathematics and Physics, The University of Queensland, Brisbane, QLD 4072, Australia

³Okinawa Institute of Science and Technology Graduate University,

Onna-son, Kunigami-gun, Okinawa, 904-095, Japan

(Dated: July 8, 2025)

Executing quantum logic in cryogenic quantum computers requires a continuous energy supply from room-temperature control electronics. This dependence on external energy sources creates scalability limitations due to control channel density and heat dissipation. Here, we propose quantum batteries (QBs) as *intrinsic* quantum energy sources for quantum computation, enabling the thermodynamic limit of zero dissipation for unitary gates. Unlike classical power sources, QBs maintain quantum coherence with their load—a property that, while theoretically studied, remains unexploited in practical quantum technologies. We demonstrate that a bosonic Fock state QB can supply the energy required for arbitrary unitary gates, regardless of the circuit’s depth, via quantum field recycling while facilitating a universal gate set controlled by a single parameter per qubit: its resonant frequency. The relative detuning of each qubit from the QB’s resonant frequency gives rise to qualitatively two gate types, off-resonance and around-resonance. The former facilitates dispersive gates which allow multi-qubit parity probing while the latter enables energy exchange between the QB and the qubits, driving both population transfer and entanglement generation. This mechanism utilizes the all-to-all connectivity of the shared-resonator architecture to go beyond the standard single- and two-qubit native gates of current platforms with gate timescales of few π/g , where g is the qubit-resonator coupling. The resultant speed-up includes also superextensive gates between symmetric Dicke states, characteristic of QB systems. By eliminating the individual drive lines, this approach significantly reduces wiring overhead, potentially quadrupling the number of qubits integrated within cryogenic systems and offering a scalable architecture for quantum computing.

I. INTRODUCTION

Quantum batteries (QBs) are defined as d -dimensional systems that store energy in their excited states while maintaining quantum coherence between the battery levels and the quantum states of their load or charger [1, 2]. Over the past decade, this concept has motivated extensive theoretical studies [2], elucidating key battery properties such as enhanced charging power [3, 4], bounds on capacity and energy storage [5, 6], and extractable work [7]. In parallel, QBs have emerged as a platform to explore collective behaviour in solid-state models [8–10] and fundamental aspects of quantum thermodynamics [11, 12].

So far, implementations of QBs have focused on demonstrating their superextensive charging property [3, 4], where the time-reversal of Dicke superradiance [13], i.e., superabsorption, scales the charging (or discharging) power per excitation as \sqrt{N} , with N being the number of battery or load quanta. This concept has been experimentally demonstrated in molecules within optical cavities [14, 15], superconducting circuits [16–18], and NMR spin systems [19], and has been theoretically proposed for cavity modes [20, 21] and many-body quantum systems [10]. However, these implementations have not yet addressed the most fundamental potential of QBs in quantum information processing: enabling reversible en-

ergy transfer that bypasses the Landauer bound by keeping the circuit’s energy requirements independent of its depth [22]. Despite the growing interest in QBs as intrinsic energy sources for quantum technologies [23], a practical platform capable of converting stored quantum energy into quantum operations remains absent.

In this work, we present the first framework for utilizing a QB as an intrinsic energy source for quantum computation. We propose a shared bosonic mode acting as the QB, coupled to the computational qubits (Fig. 1). The battery is pre-charged with sufficient energy to access the full computational Hilbert space, while energy is recycled within the closed qubit–battery system throughout the computation. In a superconducting circuit implementation using a shared-resonator QB, this approach eliminates individual drive lines per qubit, reduces heat load, and may increase qubit capacity per cryogenic system by up to fourfold. We numerically demonstrate that high-fidelity universal quantum computation remains feasible. Gates are implemented by tuning qubit resonance frequencies through multi-step protocols: either via direct energy exchange with the battery, enabling superextensive speed-up near resonance, or via virtual excitations in the dispersive regime. In the latter, we exploit qubit–battery entanglement and a phase kickback to the battery state to realize multi-qubit parity probing with a single entangling gate. Altogether, this work outlines a concrete route to integrate QBs into quantum processors, enabling energetically efficient and scalable quantum computing.

Quantum computation with QBs shows potential to

* james.quach@csiro.au

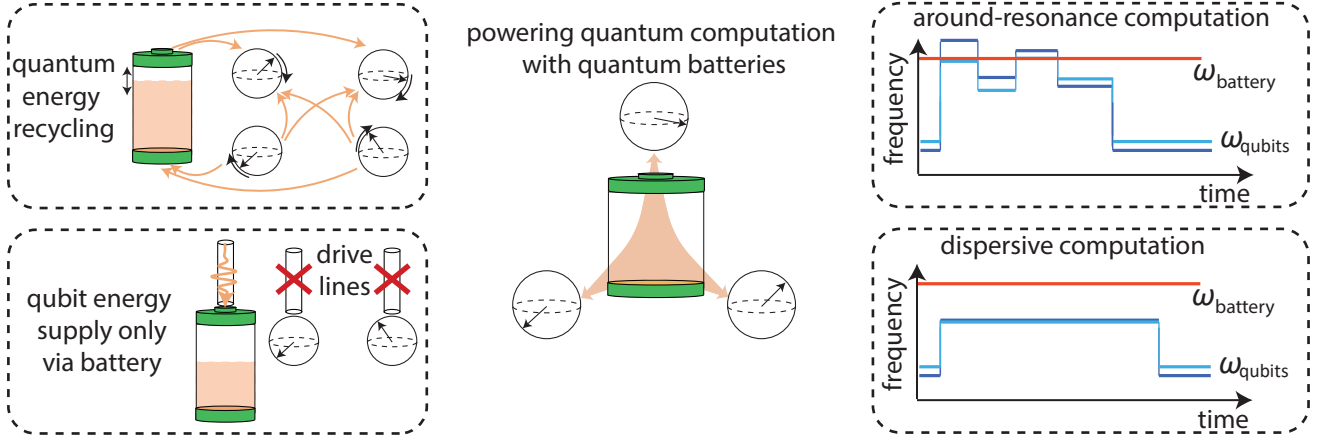


FIG. 1. Powering quantum computing with a quantum battery (QB). A bosonic mode serves as a shared QB for all computational qubits, represented by Bloch spheres (center). The battery is pre-charged with sufficient energy to implement unitary quantum logic, eliminating the need for individual drive lines (bottom left). This energy is coherently recycled throughout the computation, remaining within the closed qubit–battery quantum system (top left). Quantum computation is implemented by dynamically tuning the qubit resonance frequencies. The QB can facilitate both computation near the its resonance (top right) for rapid energy exchange, and within the dispersive regime using virtual excitations (bottom right).

reach the fundamental limit of zero active heat generation during unitary logic. The von Neumann entropy of a quantum system remains unchanged under any unitary transformation and is zero for any pure state. As a result, since entropy does not change during a unitary quantum circuit, computation can, in principle, proceed without generating heat [24]. This outcome is dictated by the thermodynamic bound $\Delta Q \geq -T\Delta S$, where ΔQ is heat generation, ΔS is entropy change, and T is temperature. Achieving this bound precisely—specifically, generating zero heat for zero entropy change—is impossible with conventional external drive pulses due to attenuation losses. However, using a QB leverages quantum field recycling [25], allowing the computation to approach this limit. This underscores the potential of QBs to enable energy-efficient quantum computation, paving the way for thermodynamically optimal quantum processing.

II. TAVIS-CUMMINGS HAMILTONIAN FOR QUANTUM COMPUTATION

To investigate how a QB can facilitate quantum information processing, we adapt the well-known Tavis-Cummings model [26] and develop it to reach dressed operators which will govern the quantum logic. The system consists of a bosonic mode acting as the QB, with frequency ω_b (denoted ω_{battery} in the figures), coupled to N two-level systems (qubits) with individual frequencies ω_i . Under the rotating wave approximation, the system is described by the Tavis-Cummings Hamiltonian

$$\hat{H} = \hbar\omega_b\hat{a}^\dagger\hat{a} + \sum_{i=1}^N \hbar\omega_i\hat{\sigma}_i^+\hat{\sigma}_i^- + \sum_{i=1}^N \hbar g_i(\hat{\sigma}_i^+\hat{a} + \hat{a}^\dagger\hat{\sigma}_i^-), \quad (1)$$

with \hat{a}^\dagger and \hat{a} being the bosonic mode's creation and annihilation operators, respectively, and g_i is the coupling constant between qubit i and the battery. The operators $\hat{\sigma}_i^+ = |1\rangle_i\langle 0|_i$ and $\hat{\sigma}_i^- = |0\rangle_i\langle 1|_i$ correspond to the raising and lowering operators of the i th qubit. The direct product of the qubit states and the boson number state, $|\vec{s}\rangle \otimes |n_b\rangle$, forms a basis of the quantum computation where n_b represents the number of quanta in the QB and $|\vec{s}\rangle = |s_0s_1\dots s_n\rangle$ are the spin projection quantum numbers of the qubits with $s_i \in \{0, 1\}$.

A key property of the Tavis-Cummings Hamiltonian is its conservation of the total excitation number operator. Because any creation (or annihilation) of a qubit excitation is accompanied by the annihilation (or creation) of quanta in the battery, $[\hat{H}, \hat{n}_{\text{ex}}] = 0$, where $\hat{n}_{\text{ex}} = \hat{a}^\dagger\hat{a} + \sum_i \hat{\sigma}_i^+\hat{\sigma}_i^-$ counts the total number of excitations in the combined QB-qubit system. As a result, the Hamiltonian is block diagonal according to the \hat{n}_{ex} value (Fig. 2). Assuming the system is initialized in the state $|0\rangle^{\otimes N} \otimes |n_{\text{ex}}\rangle$, where all qubits are in their ground state and the QB is initialized to a bosonic Fock state with $n_{\text{ex}} \geq N$, the time-evolution is confined to a single $|n_{\text{ex}}\rangle$ subspace. This subspace has dimension 2^N , and its dynamics map exactly onto the 2^N -dimensional Hilbert space of N qubits, the conventional arena for quantum computation, thereby enabling quantum computation with energy recycled entirely within the subspace. This closed-system approach shows energetically efficient computational opportunities compared to open QB implementations [27] or drive-centered computation schemes with shared resonators [28, 29].

To formalize this mapping, we introduce the dressed operators $\hat{\sigma}_{d,i}^+ = \hat{\sigma}_b^-\hat{\sigma}_i^+$ and $\hat{\sigma}_{d,i}^- = \hat{\sigma}_b^+\hat{\sigma}_i^-$, where $\hat{\sigma}_b^- = (\hat{\sigma}_b^+)^{\dagger} = \sum_{n_b} |n_b\rangle\langle n_b + 1|$ correspond to the battery annihilation operator. In Appendix A we prove that $\hat{\sigma}_{d,i}^+$

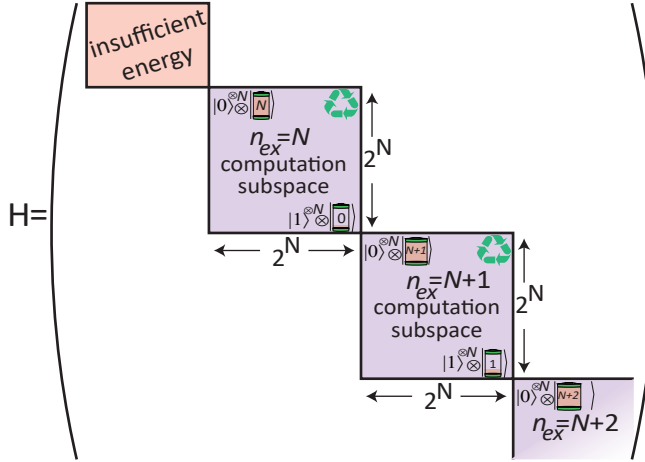


FIG. 2. The block structure of the computational subspaces. Choosing a single value for the total number of excitations in the joint QB-qubits system, n_{ex} , is sufficient to reach a computational subspace, where energy is recycled throughout the computation. When n_{ex} is smaller than the number of qubits N , the quantum battery lacks sufficient energy to support full quantum computation. Transitions between blocks are only possible through energy loss or injection of external energy.

and $\hat{\sigma}_{d,i}^-$ satisfy the Pauli algebra if $n_{\text{ex}} \geq N$ (i.e., if the battery has enough quanta to populate all qubits to their excited state). Within this n_{ex} -subspace, the system Hamiltonian can be expressed exclusively in terms of the qubit dressed operators (see Appendix A) :

$$\hat{H}_{n_{\text{ex}}} = \sum_{i=1}^N \hbar \Delta_i \hat{\sigma}_{d,i}^+ \hat{\sigma}_{d,i}^- + \sum_{i=1}^N \hbar g_i \left(\hat{\sigma}_{d,i}^+ \sqrt{n_{\text{ex}} - \hat{n}_q} + \sqrt{n_{\text{ex}} - \hat{n}_q} \hat{\sigma}_{d,i}^- \right) \quad (2)$$

Here, $\Delta_i = \omega_i - \omega_b$ represents the frequency detuning between qubit i and the battery, \hat{n}_{ex} is treated as a scalar due to its conservation, and $\hat{n}_q = \sum_i \hat{\sigma}_{d,i}^+ \hat{\sigma}_{d,i}^- = \sum_i \hat{\sigma}_i^+ \hat{\sigma}_i^-$ is the (dressed) qubit total excitation operator. All quantum information processing presented in this paper is performed using Eq. (2) by manipulating Δ_i as a function of time and assuming $g_i = g$ for all qubits. This scheme is readily generalized to a distribution of g values and even to their modulation as in tunable-coupler systems [30].

The interaction term in Eq. (2) encompasses the unique features of performing computation with QBs. The QB forces non-local computation when coupled to all qubits. The inseparability between \hat{n}_q and $\hat{\sigma}_{d,i}^\pm$ indicates that the state of all qubits will determine which gate is implemented given a specific set of Δ_i values and gate duration. This effect creates a native all-to-all interaction and high-degree of entanglement between the qubits. Still, we show below that a universal gate set is achievable solely through energy detuning, and separable

gates can be implemented through several detuning steps to all qubits, even those who are idled.

III. QUANTUM BATTERY FEATURES

A hallmark characteristic of QBs is their superextensive speed-up in energy transfer [3, 4, 14]. We analyse the implication of this property on quantum computation when setting $\Delta_i = 0$ for all qubits, reducing the Hamiltonian to $\hbar g \sum_{i=1}^N (\hat{\sigma}_{d,i}^+ \sqrt{n_{\text{ex}} - \hat{n}_q} + \sqrt{n_{\text{ex}} - \hat{n}_q} \hat{\sigma}_{d,i}^-)$. For a single-qubit case, this Hamiltonian simplifies to $\hbar g \sqrt{n_{\text{ex}}} \hat{\sigma}_{d,i}^x$, recovering the expected Jaynes-Cummings result of executing an X gate after $t = \pi/(2g\sqrt{n_{\text{ex}}})$ interaction time. This case can be generalized to any QB-qubit interaction where only qubit i is on-resonance and the others are highly off-resonance so that an initial state of $|n_b\rangle \otimes |0\rangle_i$ in the QB-qubit subspace reaches $|n_b - 1\rangle \otimes |1\rangle_i$ in $t = \pi/(2g\sqrt{n_b})$ (dashed line in Fig. 3a).

The superextensive speed-up, shown in Fig. 3a, arises as qubits are added to the system, enabling reduced collective gate times for mapping any two symmetric Dicke states of the system, such as $|0\rangle^{\otimes N} \leftrightarrow |1\rangle^{\otimes N}$. The gate time decreases when increasing the number of qubits, assuming a fixed number of battery quanta per qubit (n_b/N) in the initial state $|n_b\rangle \otimes |0\rangle^{\otimes N}$. Increasing this ratio will reduce the gate time, eventually converging to the superextensive speed-up limit of $1/\sqrt{N}$. The time-reversal of the simulated gate is the famous Dicke superradiance, which was demonstrated in many quantum computation platforms with a vacuum state shared-mode [31, 32]. Our scheme shows a use case in which QBs harness the collective effects of superradiance and superabsorption to accelerate quantum computation.

Another famous feature of QBs comes from the increased precision of these collective gates when increasing the number of qubits [20]. Fig. 3b presents that when the QB is initialized in the Fock state, the gate error values are between 10^{-2} and below 10^{-3} (blue shades in Fig. 3b). Such values are unattainable when the QB is initialized in a coherent state, where the n_b values are coherently distributed in the initial state (green shades in Fig. 3b). These results highlight the importance that the QB be initialized in a quantum state of light [33, 34]) rather than a coherent state, overcoming previous bounds on the gate fidelities and minimal energy requirements which assumed an external coherent energy source [35] or a QB which is separable to the qubit system [22].

Fig. 3 demonstrates a specific state mapping that passes through Dicke symmetric states (bright states). A separable superexpensive $X^{\otimes N}$ gate can be achieved in the limit of $n_b \gg N$ (with a Taylor expansion in Eq. (2)). However, a small Fock number is critical to increase the QB lifetime which scales as $1/n_b$ [33]. Therefore, the circuit examples presented in the following sections uses $n_b/N < 2$ to reach low-error unitary computation, by optimizing the detuning values over multiple steps.

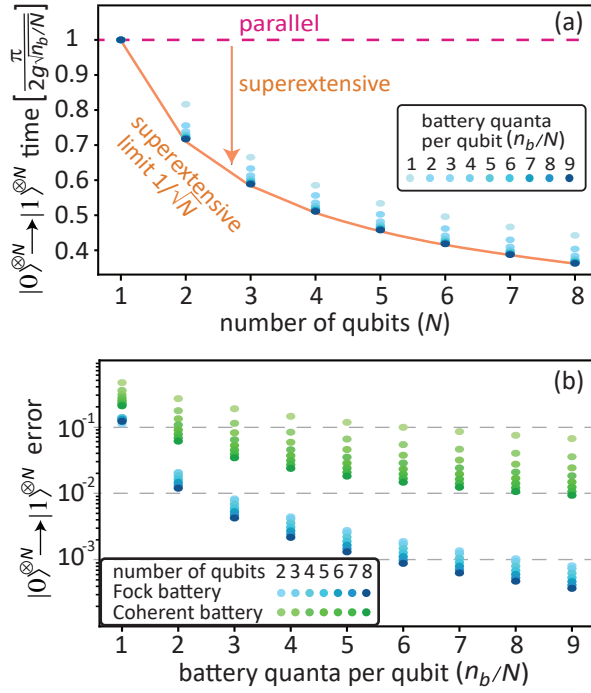


FIG. 3. Superextensive scaling in a specific qubit gate. (a) Collective $|\langle 0 \rangle^{\otimes N} \rightarrow \langle 1 \rangle^{\otimes N}|$ gate time for different battery-quanta-per-qubit ratios (blue dots), normalized to the parallel charging time. The reference parallel time corresponds to N separate batteries, each coupled to a single qubit (pink dashes). Values below 1 indicate superextensive speed-up where collective multi-qubit interactions reduce gate times by increasing the number of qubits given a fixed n_b/N ratio, until reaching the superextensive speed-up limit of $1/\sqrt{N}$ (orange). (b) The collective $|\langle 0 \rangle^{\otimes N} \rightarrow \langle 1 \rangle^{\otimes N}|$ error as a function of the initial number of quanta in the battery when the battery initialized in a Fock state (blue shades) and in a coherent state (green shades). The Fock state QB exhibits significantly better performance than the coherent-state QB, with gate error decreasing further as more qubits are added to the system. In both (a) and (b), all qubits are on-resonance with the QB.

IV. QUANTUM INFORMATION PROCESSING WITH A QUANTUM ENERGY SOURCE

A. Universal quantum gate set in the closed Battery —qubits system

Reaching a universal quantum gate set hinges on performing arbitrary local single-qubit gates while idling the other qubits and entangling every pair of qubits in the system. An entangling \sqrt{i} SWAP gate is implemented by detuning the qubit pairs from the mode's resonance by a similar frequency Δ in the dispersive regime, when $\Delta \gg g\sqrt{n_{\text{ex}}}$. This scheme is commonly used in ions [36], but was also implemented in superconducting qubits [37] and spin qubits [38, 39]. Arbitrary Z rotations can be implemented by detuning the resonance of a single qubit compared to the other. Thus, reaching a single local

energy-changing gate (which is not a trivial $|0\rangle \leftrightarrow |1\rangle$ mapping) is sufficient to complete the generator set of all single-qubit operations [40]. Such a gate may be a Hadamard, a \sqrt{X} , or any non-trivial rotation that modifies the qubit's energy. Although these gates typically yield high fidelities in conventional quantum computation, they become challenging in a collective system.

We numerically show that the universal gate set can be completed by reaching a similar battery-qubit energy exchange gate regardless of the state of the other qubits. That is, implementing the same gate when the single-qubit-battery subsystem includes all values from n_{ex} quanta, down to $n_{\text{ex}} - N + 1$ quanta. In Appendix C and Fig. 7 we demonstrate that few detuning steps are sufficient to implement a local non-trivial energy-changing gate that produces the same unitary independently on the other qubits. In our study, including examples with up to five qubits and n_{ex} of up to seven excitations, two detuning steps were used to achieve average gate fidelities of above 99.5% and worst-case fidelities of 99%.

In our implementation, a universal gate set relies on using several detuning steps in order to increase the available degrees of freedom. Thus, increasing the number of steps can further enhance these single-qubit fidelities and, moreover, enable multi-qubit gates with high fidelity. From a theoretical standpoint, the QB system can implement any N -qubit unitary using $M \geq (4^N - 1)/(N + 1)$ detuning steps, since M times the total degrees of freedom per step, $(N + 1)$, accede the N -qubit unitary degrees of freedom. In practice, however, our simulations for a five qubit system only required two detuning steps for demonstrating a universal gate set.

B. Multi-qubit parity-probing in the dispersive regime

Entangling multiple qubits is natural to the QB-qubit system given the nonlocal Hamiltonian in Eq. (2). In this section we present an analytic description that shows how the QB's state affects the entangling gates in the dispersive regime. Specific cases of these gates were implemented when the bosonic cavity was initially empty (i.e., in the vacuum state) to generate Greenberger–Horne–Zeilinger (GHZ) states using a single dispersive gate with ten [37], and twenty [41] qubits. These interactions implement either an iSWAP gate or a \sqrt{i} SWAP gate when the gate is applied for $t = \pi/(2g^2/\Delta)$ or $t = \pi/(4g^2/\Delta)$, respectively. We show that populating the QB creates additional degrees of freedom for the executed entangling gate, which in turn allow a phase kickback to the battery due to battery-dependent gates.

In Appendix B we derive from Eq. (2) the dispersive Hamiltonian [42–44]

$$\hat{H}_{\text{disp}} \approx \left(\Delta + \frac{2g^2}{\Delta} (n_{\text{ex}} - N/2 + \hat{J}^z) \right) \hat{J}^z - \frac{g^2}{\Delta} \hat{J}^- \hat{J}^+, \quad (3)$$

using the collective angular momentum operators, $\hat{J}^z = \frac{1}{2} \sum_{i=1}^N \hat{\sigma}_{d,i}^z = N/2 - \hat{n}_q$, and $\hat{J}^\pm = \sum_{i=1}^N \hat{\sigma}_{d,i}^\pm$. The exchange term $\hat{J}^- \hat{J}^+$ creates interactions between qubit states with similar number of qubit excitations. A full exchange of quanta occurs when the interaction is applied for $t_{\text{disp}} = \pi/(2g^2/\Delta)$, regardless of the QB's state. However, the QB's state and the detuning value do influence the relative phases of different \hat{J}^z values. These relative phases exhibit jumps of $\pi/2$ when the ratio Δ^2/g^2 is an integer (as was shown in ion-based systems [45]) and jumps of π according to the parity of n_{ex} . Taking a two-qubit example, the dispersive gate is

$$U_{\text{disp}}(n_{\text{ex}}, \Delta) = \exp(-i\hat{H}_{\text{disp}}t_{\text{disp}}) = \quad (4)$$

$$\begin{pmatrix} (-1)^{n_{\text{ex}}} & 0 & 0 & 0 \\ 0 & 0 & -i\Delta^2/g^2 & 0 \\ 0 & -i\Delta^2/g^2 & 0 & 0 \\ 0 & 0 & 0 & -(-1)^{n_{\text{ex}}+\Delta^2/g^2} \end{pmatrix}$$

which implements an iSWAP gate when $\Delta^2/g^2 \bmod 4 = 3$ and n_{ex} is even.

These degrees of freedom in the QB-qubit system can be utilized for probing a multi-qubit parity with a single entangling gate, as exemplified for a two-qubit probing in Fig. 4a. The protocol starts with entangling an ancillary qubit (q_2) with the QB using a $\pi/2$ energy-transfer gate, so that the combined subspace of the QB and the to-be-probed qubits reaches an n_{ex} superposition of even and odd values (corresponding to the $|0\rangle$ and $|1\rangle$ ancillary qubit state). Subsequently, the entangling gate becomes a controlled-parity unitary gate when applied for $t = t_{\text{disp}}$, where the controlling qubit is the ancillary qubit:

$$U = \frac{1}{2} U_{\text{disp}}(n_{\text{ex}}) \left(|0_a\rangle\langle 0_a| \otimes I + |1_a\rangle\langle 1_a| \otimes (U_{\text{disp}}(n_{\text{ex}}))^{-1} U_{\text{disp}}(n_{\text{ex}} - 1) \right) \quad (5)$$

We derive in Appendix B that $(U_{\text{disp}}(n_{\text{ex}}))^{-1} U_{\text{disp}}(n_{\text{ex}} - 1) = e^{2it_{\text{disp}}g^2/\Delta \hat{J}^z} = i^{N_{\text{disp}}} Z^{\otimes N_{\text{disp}}}$ with N_{disp} being the number of qubits involved in the dispersive gate. Thus, this gate creates a phase kickback to the ancillary qubit, due to its entanglement with the QB. The protocol finishes by applying a disentangling $\pi/2$ gate between the ancillary qubit and the battery to establish a direct mapping between the N -qubit parity and the ancillary qubit state, and with another dispersive gate to bring back the probed qubits into their original state. Overall, the system can probe any $Z^{\otimes N_{\text{disp}}}$ parity operator with a single collective gate, independent of the QB's state and the number of qubits. This property is particularly attractive for quantum error correction, which requires frequent probing of multi-qubit parity operators.

Figures 4 demonstrate a specific circuit (a) and its simulated implementation (b) when probing a two-qubit parity. In this simulation, we chose an $I \otimes I \otimes H$ gate to create

an entanglement between q_2 and the battery and then to disentangle them after the controlled-parity gate. The dispersive gate implements CZ and SWAP gates, which are accompanied with a set of local Z gates if qubit q_2 is in the $|1\rangle$ state. Eight detuning steps were used to implement the $I \otimes I \otimes H$ gate with an overall duration of $0.5\pi/2g$ (inset of Fig. 4b). Then, $q_{0,1}$ were detuned to $\Delta = 27.5g$ for a duration of $27.5\pi/2g$, and q_2 was heavily detuned to minimize its effect. When comparing the simulated circuit with a ideal parity-probing circuit (Fig. 4a), we find a Hilbert-Schmidt distance of 0.642, corresponding to an average circuit fidelity of 95.4% (simulation details found in Appendix E). Fidelity could be further improved by allowing for the continuous, non-adiabatic time-evolution of the qubit detunings, offering additional control beyond the idealized instantaneous detuning scheme we have so far considered.

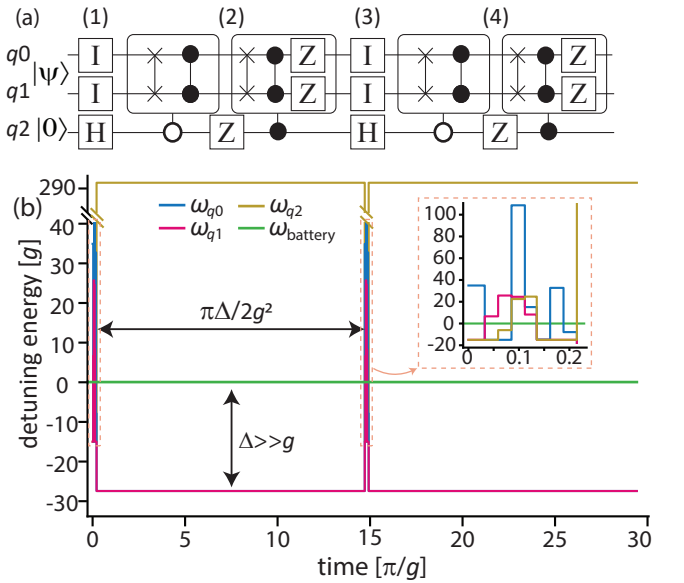


FIG. 4. Multi-qubit parity probing through battery-dependent dispersive gates. (a) The protocol for probing multi-qubit parities through dispersive interactions, exemplified with a 2-qubit probing circuit. Step (1) entangles the ancillary qubit (q_2) with the battery. Step (2) applies a battery-dependent dispersive gate that implements a superposition of $U_{\text{disp}}(n_{\text{ex}})$ and $U_{\text{disp}}(n_{\text{ex}} - 1)$ in the joint battery-two-qubit subspace. Step (3) maps the parity of $|\psi\rangle$ onto the ancillary qubit, producing $|\psi\rangle_{\text{even}} |1\rangle_{q_2} + |\psi\rangle_{\text{odd}} |0\rangle_{q_2}$, where $|\psi\rangle_{\text{even}}$ and $|\psi\rangle_{\text{odd}}$ are the even and odd components of $|\psi\rangle$, respectively. Step (4) restores the probed qubits to their original state $|\psi\rangle$. This sequence remains unchanged when generalizing from two-qubit to N -qubit parity probing. (b) Implementation of the circuit in (a) using only qubit frequency detunings, for $n_{\text{ex}} = 5$. Each dispersive gate requires $(\Delta/\pi) \times \pi/(2g)$ time units (with $\Delta = 27.5g$), independent of the number of qubits probed. The $I \otimes I \otimes H$ gate takes approximately $(1/2) \times \pi/(2g)$, implemented here in 8 steps (inset), and is expected to shorten with a more highly charged battery.

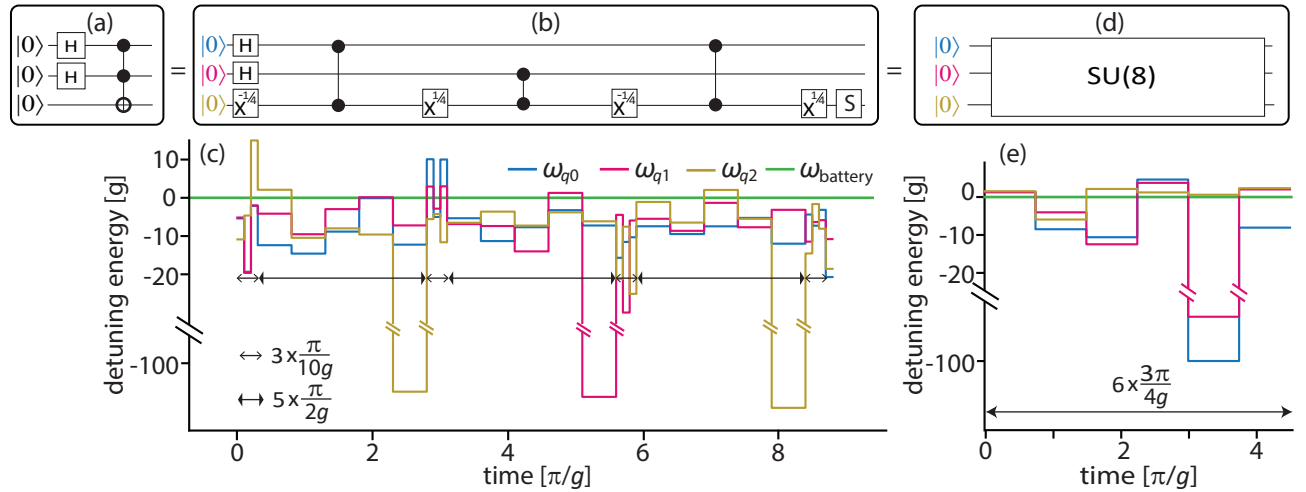


FIG. 5. Computation via battery-mediated multi-qubit interactions near resonance. (a) Target circuit featuring a three-qubit Toffoli gate, applied after preparing the control qubits in superposition. (b) The standard decomposition of the target circuit into a sequence of single-qubit and pairwise entangling gates. (c) Implementation of (b) yielding a final infidelity of 3×10^{-3} . Energy-changing operations (thin arrows) are realized in three detuning steps, each with a duration of $\pi/10g$, while entangling operations (thick arrows) require five steps, each of duration $\pi/2g$, to account for round-trip energy exchange via the battery. (d) Uniting the full target circuit into a single multi-qubit unitary. (e) Direct implementation of the unitary in (d) using six steps of duration $3\pi/4g$, reaching an infidelity of 3×10^{-9} while significantly reducing the total circuit time compared to (c).

C. Multi-qubit unitary gates through direct battery—qubit interactions

In the previous section, we have shown how the state of the QB and its entanglement degrees with the qubits can be utilized for unique processing. However, the timescales of the dispersive gates introduced significant errors in their experimental implementation, especially when increasing the number of qubits [41]. This effect motivated efforts to find new computation schemes for shared-resonator quantum computers using driven cavities [29]. In this section, we show that the QB can facilitate computation without reaching the dispersive regime timescales, but rather through direct interactions between the QB and the qubits, reaching overall unitary durations of a few π/g .

Figure 5a presents a circuit example which involves energy transfer from the QB to the qubits and a non-Clifford three-qubit entangling gate in the form of a Toffoli gate. In conventional quantum processors, this circuit is broken down to the hardware’s native gates as shown in Fig. 5b. We start with a similar approach to implement the circuit using an interleaved sequence of energy-transfer gates and entangling CZ gates, shown in Fig. 5c. We implement each energy-transfer gate in three $0.1\pi/g$ steps, which reach high fidelities but do not exhibit a superextensive speed-up, since the state mapping is not necessarily between two symmetric Dicke states. An on-resonance superextensive gate that transfers half a quanta in the case of $n_{\text{ex}} = 5$ and $N = 3$ should take $1/(2\sqrt{5/3}) \cdot \pi/2g \approx 0.2\pi/g$. The CZ gates were implemented through five steps of $\pi/2g$, intuitively to enable a back-and-forth interaction between two qubits via the

battery. Overall, this simulation implemented the circuit with an overall infidelity of 3×10^{-3} , where the detuning parameters were chosen to optimize the fidelity.

Figure 5e shows that the overall circuit time can be further reduced and the implementation can be simplified when combining the whole circuit into a single SU(8) unitary (Figure 5d) implemented in few detuning steps. Specifically, we use six $3\pi/4g$ steps to reach an infidelity of 3×10^{-9} with an overall duration of $4.5\pi/g$. This example shows that the shared-resonator can combine multi-qubit entangling and energy transfer from the QB to the qubits within the same sequence. This property can open paths to new computation methods with smaller circuit depth that utilize the all-to-all connectivity of the shared-resonator architecture, as opposed to a shared-resonator pairwise computation [29].

V. SCALING OPPORTUNITIES AND ENERGETIC EFFICIENCY

Powering quantum computers with QBs offer a unique opportunity to scale cryogenic processors by enabling full qubit control through flux lines and supplying all unitary gate energy prior to computation. The inset of Fig. 6a illustrates the key differences between conventional and QB architectures: in the QB approach, the qubits are connected to a shared-resonator and without individual qubit drive lines which generate active and passive heat during conventional computation. This reduction in heat sources increases the potential number of qubits per cryogenic fridge, addressing a critical scalability bottleneck for cryogenic computers.

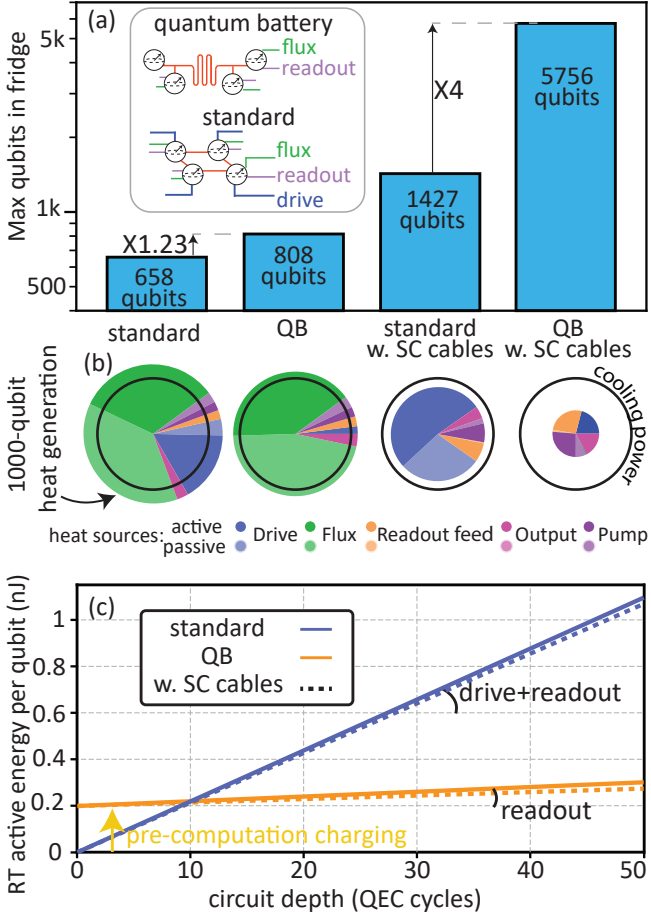


FIG. 6. Scaling opportunities and energy requirements of the QB architecture with superconducting qubits. (a) The maximum number of qubits that the state-of-the-art cryogenic fridge can support, derived from the minimal number of qubits that reach the cooling power. The QB configuration enabled a factor of 1.23 additional qubits with available cables, while superconducting flux lines will enable increasing the number of qubits by a factor of 4 compared to the standard configuration (with superconducting cables). Inset: The QB (top) and the conventional (bottom) architectures. The conventional computation includes an additional control line per qubit (drive) and corresponding attenuators which create passive and active heat during the computation. (b) Distribution of heat sources at the cryogenic fridge limiting levels. The pie chart's area represents the total heat power of a thousand qubits compared to the cooling power (black). (c) The accumulated room-temperature (RT) energy per qubit that is required for the input control lines as a function of the circuit depth. Although the QB requires charging prior to the computation, removing the drive pulses keep the additional energy to be dominated by readout and the QB computation becomes energetically efficient after few quantum error correction (QEC) cycles. Detailed derivation of (a,b) is provided in Appendix D.

By comparing the total heat load to the state-of-the-art cooling capacity of cryogenic fridges, we assess the potential scaling advantages of the QB architecture, as illustrated in Fig. 6a. To evaluate how flux-only control affects scalability, we estimated the heat power dissipated at the two coldest stages of a dilution refrigerator during quantum computation, following the methodology of Krinner et al. [46] (see Appendix D and Fig. 8 for details). Figure 6b displays the total heat generated by a 1000-qubit system (represented by the area of the pie chart), from which the maximum number of qubits per fridge can be inferred by comparing to the fridge's available cooling power (black).

We calculated the active and passive heat contributions from control lines based on standard pulse usage (colored segments in Figure 6b). This analysis revealed that with current cable technology, adopting a QB architecture can increase the number of qubits per fridge by 23%, with the dominant limitation being attenuation along the flux lines at the mixing chamber stage. If superconducting cables are used for the flux lines, the scaling potential improves dramatically: we observe an 8.75-fold increase compared to the standard configuration and a 4-fold improvement compared to a conventional setup with superconducting cables. These gains are not achievable if drive lines are retained, as their associated attenuators generate heat which prevent the use of superconducting materials. In the QB configuration with superconducting cables, heat dissipation is primarily due to the readout components, including feed lines and amplifier pumps, while the remaining heat arises from passive dissipation along the single drive line per battery (assuming each battery controls 10 qubits).

In addition to the quantum computer scaling opportunities, QBs reduce the total active energy consumption of the quantum computation. To quantify this, we calculate the active power that enters the cryogenic fridge to estimate the computation's input energy at room temperature (detailed in Appendix D). The results, presented in Fig. 6c, show that the QB architecture becomes more energy-efficient than conventional designs once the circuit depth exceeds the energy cost of preparing the QB in the Fock state. We conservatively estimate this preparation energy as equivalent to that required energy for driving and reading out 10 qubits over 10 quantum error correction (QEC) cycles, based on the energy needed to overcome competing losses [47].

Once initialized, the QB architecture eliminates drive-pulse energy consumption during computation by extending the concept of quantum field recycling [25], leaving only readout pulses as an energy input. Consequently, the energy per circuit depth accumulates slower than in conventional architectures, and the energy consumption gap between the two approaches widens as the circuit depth increases. At a fundamental level, QEC protocols use mid-circuit readout to stabilize the qubits, so that the only energy entering the system during QB-based computation is used solely to remove entropy.

VI. DISCUSSION

In this manuscript, we presented the first practical framework for integrating QBs as intrinsic energy sources for quantum technologies, in particular for quantum computation. We demonstrated that a shared bosonic mode, pre-charged into a quantum state, can enable universal quantum computation through frequency detuning alone, including single- and multi-qubit gates as well as controlled-parity operations. By recycling energy within a closed QB-qubit system, our scheme approaches the thermodynamic limit where energy is consumed only during readout. In cryogenic platforms, eliminating individual drive lines enables a scalable control architecture built from standard components, offering a practical alternative to more complex scalability proposals such as photonic links[48].

Several challenges remain before large-scale QB-based quantum computing can be realized. High-fidelity Fock state preparation is still under active development [34, 49, 50], and optimal battery charging is expected to need an ancillary nonlinear element [21]. To execute computations, we optimized flux parameters using off-the-shelf routines in our simulations; however, scaling this process to larger systems may demand more advanced optimization and calibration methods. In a practical setting, stable gate operation will benefit from real-time feedback control to counter flux drifts and from smooth flux profiles that avoid signal ringing or overshoot [51]. Importantly, our protocol reaches circuit timescales on the order of π/g , allowing for fast entangling gates outside the dispersive regime. This helps reduce the impact of noise sources such as collective decay [52], Fock states decay [33], and charge noise, which is further suppressed when eliminating drive lines.

The proposed QB architecture is compatible with existing quantum hardware. The bosonic mode can be implemented using electromagnetic resonators in superconducting [29, 41, 53] or semiconductor spin [38, 39] processors, or motional modes in ion traps[36]. While shared-resonator architectures have been employed in earlier demonstrations of entangling gates [53] and GHZ states generation [37], these implementations operated in the dispersive regime and maintained the resonator in the vacuum state, without exploiting it as an active energy source. To our knowledge, this is the first proposal to harness stored quantum energy in a bosonic mode to perform quantum logic, relying solely on frequency detuning.

Our approach is facilitated by a simplified control and reduced thermal load. Removing a dedicated drive line per qubit at cryogenic temperature eliminates two associated lines per qubit at room temperature, thereby lowering system complexity and minimizing signal crosstalk [54]. Moreover, traditional analog drive control requires high precision that requires a significant electronic overhead that in turn force the electronics to remain at room temperature. In contrast, frequency-based control aligns naturally with emerging cryogenic-compatible technolo-

gies, such as cryo-CMOS [55] or single-flux-quantum logic [56], offering additional reductions in power consumption. In addition, integrating QBs with efficient readout methods, such as microwave photomultipliers [57], can further enhance the scaling potential. Altogether, incorporating QBs into quantum processors represents a promising pathway toward simpler, more scalable, and energetically favorable quantum computation.

ACKNOWLEDGMENTS

K.H. and J.Q.Q. acknowledge funding from the Revolutionary Energy Storage Systems Future Science Platform.

DATA AVAILABILITY

The data of this study, as well as the code used to generate the figures, are openly available [58].

Appendix A: The Tavis-Cummings Hamiltonian with dressed operators

In this appendix, we derive the dressed-operator Hamiltonian in Eq. (2) from the conventional TC Hamiltonian in Eq. (1). Then, we will show the conditions in which the dressed operators follow Pauli algebra. Using the same notations as in Section II, we see that the QB creation operator $\hat{\sigma}_b^+ = \sum_{n_b} |n_b + 1\rangle \langle n_b|$ satisfies

$$\hat{a}^\dagger |n_b\rangle = \sqrt{n_b + 1} |n_b + 1\rangle = \sqrt{\hat{n}_b} |n_b + 1\rangle = \sqrt{\hat{n}_b} \hat{\sigma}_b^+ |n_b\rangle. \quad (\text{A1})$$

Eq. A1 uses the theorem that if $|\psi\rangle$ (in our case $|n_b + 1\rangle$) is an eigenstate of an operator \hat{O} (here \hat{n}_b) with eigenvalue λ (here $n_b + 1$), then $|\psi\rangle$ is also an eigenstate of a function of the operator, $f(\hat{O})$ (here $\sqrt{\hat{n}_b}$), with eigenvalue $f(\lambda)$ (i.e., $\sqrt{n_b + 1}$) when $f(x)$ is smooth (see proof by power series in [59], Sec. 1.9, p. 54). Then, we find that the interacting terms in this TC Hamiltonian obey

$$\hat{a}^\dagger \hat{\sigma}_i^- |\vec{s}, n_b\rangle = \sqrt{\hat{n}_b} \hat{\sigma}_i^- |\vec{s}, n_b\rangle = \sqrt{\hat{n}_{\text{ex}} - \hat{n}_q} \hat{\sigma}_b^+ \hat{\sigma}_i^- |\vec{s}, n_b\rangle, \quad (\text{A2})$$

and similarly, by taking the Hermitian conjugate

$$\hat{\sigma}_i^+ \hat{a} = \hat{\sigma}_i^+ \hat{\sigma}_b^- \sqrt{\hat{n}_{\text{tot}} - \hat{n}_q}, \quad (\text{A3})$$

where $(\sqrt{\hat{n}_{\text{tot}} - \hat{n}_q})^\dagger = \sqrt{\hat{n}_{\text{tot}} - \hat{n}_q}$ since $\hat{n}_{\text{tot}} - \hat{n}_q$ is diagonal.

By substituting these equalities to the TC Hamiltonian from Eq. (1), in addition to $\hat{a}^\dagger \hat{a} = \hat{n}_{\text{ex}} - \hat{n}_q$, and $\omega_i =$

$\Delta_i + \omega_b$, the system's Hamiltonian is written as

$$\hat{H} = \omega_b \hat{n}_{ex} + \sum_{i=1}^N \Delta_i \hat{\sigma}_i^+ \hat{\sigma}_i^- + \sum_{i=1}^N g_i \left(\hat{\sigma}_b^- \hat{\sigma}_i^+ \sqrt{\hat{n}_{ex} - \hat{n}_q} + \sqrt{\hat{n}_{ex} - \hat{n}_q} \hat{\sigma}_b^+ \hat{\sigma}_i^- \right), \quad (\text{A4})$$

showing how all qubits interact with each other in a non-linear manner through the battery.

Our first assumption for the rest of this appendix is that the initial state of the system is $|0\rangle^{\otimes N} \otimes |n_{ex}\rangle$, corresponding to the ground state of the qubit system and a Fock-state with n_{ex} excitations in the resonator. As discussed in section II, this assumption keeps the calculation within a single block of the Hamiltonian, creating a direct mapping between the qubits' state and the number of battery excitations. Only under this assumption, we can consider \hat{n}_{ex} as a scalar n_{ex} throughout the derivation and simulations within this manuscript.

Finally, we show that the Hamiltonian from Eq. (A4) converges to Eq. (2). First, we substitute the dressed operators from section II, $\hat{\sigma}_{d,i}^+ = \hat{\sigma}_b^- \hat{\sigma}_i^+$ and $\hat{\sigma}_{d,i}^- = \hat{\sigma}_b^+ \hat{\sigma}_i^-$. Second, since $\hat{\sigma}_b^- \hat{\sigma}_b^+ = \mathbb{I}_b$ (the identity in the battery subspace),

$$\hat{\sigma}_i^+ \hat{\sigma}_i^- = \hat{\sigma}_i^+ \hat{\sigma}_i^- \hat{\sigma}_b^- \hat{\sigma}_b^+ = \hat{\sigma}_b^- \hat{\sigma}_i^+ \hat{\sigma}_i^- \hat{\sigma}_b^+ = \hat{\sigma}_{d,i}^+ \hat{\sigma}_{d,i}^-,$$

so that the local qubit operators and \hat{n}_q can be expressed in terms of $\hat{\sigma}_{d,i}^+ \hat{\sigma}_{d,i}^-$. Finally, a full convergence to Eq. (2) is reached when neglecting the first term in Eq. (A4) as it is now a global phase to all states within the subsystem.

To show that the dressed operators follow Pauli algebra, we calculate the commutation relations,

$$\begin{aligned} [\hat{\sigma}_{d,i}^+, \hat{\sigma}_{d,i}^-] &= [\hat{\sigma}_b^-, \hat{\sigma}_i^+, \hat{\sigma}_b^+ \hat{\sigma}_i^-] \\ &= [\hat{\sigma}_b^-, \hat{\sigma}_b^+] \hat{\sigma}_i^- \hat{\sigma}_i^+ + \hat{\sigma}_b^- \hat{\sigma}_b^+ [\hat{\sigma}_i^+, \hat{\sigma}_i^-] \\ &= |0_i, 0_b\rangle \langle 0_i, 0_b| + [\hat{\sigma}_i^+, \hat{\sigma}_i^-], \end{aligned} \quad (\text{A5})$$

where $|0_i, 0_b\rangle$ denotes the joint vacuum state of qubit i and the bosonic mode. Therefore, the operators $\hat{\sigma}_{d,i}^+$ and $\hat{\sigma}_{d,i}^-$ preserve Pauli algebra only if the state $|0_i, 0_b\rangle$ is excluded from the subsystem. This condition is satisfied by assuming $n_{ex} \geq N$ (i.e., the eigenvalue of \hat{n}_{ex} is at least the number of qubits), ensuring that zero photons in the cavity occur only when the qubits are in the state $|1\rangle^{\otimes N}$ and $n_{ex} = N$. Under this assumption, which is also necessary for the system to access the full qubit Hilbert space during computation,

$$[\hat{\sigma}_{d,i}^+, \hat{\sigma}_{d,i}^-] = [\hat{\sigma}_i^+, \hat{\sigma}_i^-].$$

These commutation relations allow us to define effective Pauli operators as

$$\begin{aligned} \hat{\sigma}_i^x &= \hat{\sigma}_{d,i}^+ + \hat{\sigma}_{d,i}^- & \hat{\sigma}_i^y &= i \left(\hat{\sigma}_{d,i}^+ - \hat{\sigma}_{d,i}^- \right) \\ \hat{\sigma}_i^z &= \hat{\sigma}_{d,i}^- \hat{\sigma}_{d,i}^+ - \hat{\sigma}_{d,i}^+ \hat{\sigma}_{d,i}^-, \end{aligned}$$

which satisfy all standard Pauli operator identities and commutation relations.

Appendix B: The dispersive Hamiltonian and the Controlled-Unitary gate

1. Converting to the angular momentum basis

To find an analytical solution for collective entangling gates, it is convenient to transform Eq. (2) to a Hamiltonian with collective operators, assuming all involved qubits are detuned by the same Δ . The collective operators $\hat{J}^{x,y,z} = \frac{1}{2} \sum_{i=1}^N \hat{\sigma}_{d,i}^{x,y,z}$ satisfy the angular momentum algebra, $[\hat{J}^i, \hat{J}^j] = i \epsilon_{ijk} \hat{J}^k$, where ϵ_{ijk} is the Levi-Civita tensor, and

$$\hat{J}^\pm = \sum_{i=1}^N \hat{\sigma}_{d,i}^\mp = \sum_{i=1}^N (\hat{\sigma}_{d,i}^x \pm i \hat{\sigma}_{d,i}^y) = 2(\hat{J}^x \pm i \hat{J}^y).$$

Note that the sign flip between $+$ and $-$ arises because $|0\rangle^{\otimes N} = |J = N/2, m_J = J\rangle$, so $\hat{\sigma}_i^+$ increases excitations but reduces m_J . Additionally, $\hat{n}_q = \sum_{i=1}^N \frac{1-\hat{\sigma}_i^z}{2} = \frac{N}{2} - \hat{J}^z$, so that the Hamiltonian becomes

$$\begin{aligned} \hat{H} &= -\Delta \left(\frac{N}{2} - \hat{J}^z \right) \\ &+ g \left(\hat{J}^- \sqrt{n_{ex} - \frac{N}{2} + \hat{J}^z} + \sqrt{n_{ex} - \frac{N}{2} + \hat{J}^z} \hat{J}^+ \right), \end{aligned} \quad (\text{B1})$$

The states $|J, m_J\rangle$ form the natural basis, where $-J \leq m_J \leq J$, with $\hat{J}^z |J, m_J\rangle = m_J |J, m_J\rangle$ and $\hat{J}^\pm |J, m_J\rangle = \sqrt{(J \mp m_J)(J \pm m_J + 1)} |J, m_J \pm 1\rangle$. Since \hat{J}^2 remains constant under Eq. (B1), the mixture of J values is the source of the collective entangling gates.

For a more compact notation, define the operator

$$\hat{A} = \sqrt{(n_{ex} - N/2) \mathbb{I} + \hat{J}^z}, \quad (\text{B2})$$

which satisfies $\hat{A} |J, m_J\rangle = \sqrt{(n_{ex} - N/2) + m_J} |J, m_J\rangle$, and $[\hat{A}, \hat{J}^z] = 0$. Removing the global phase $-\Delta N/2$ gives the simplified Hamiltonian:

$$\hat{H} = \Delta \hat{J}^z + g \left(\hat{J}^- \hat{A} + \hat{A} \hat{J}^+ \right), \quad (\text{B3})$$

that we use to analyze the dispersive gates.

2. The Schrieffer–Wolff Transformation

To understand native dispersive gates, we now perform the Schrieffer–Wolff transformation. For a Hamiltonian $\hat{H} = \hat{H}_0 + \hat{V}$ with $|\hat{V}| \ll |\hat{H}_0|$, the transformed Hamiltonian is approximated by

$$\hat{H}' = e^{\hat{S}} (\hat{H}_0 + \hat{V}) e^{-\hat{S}} \approx \hat{H}_0 + \frac{1}{2} [\hat{S}, \hat{V}],$$

where \hat{S} satisfies $\hat{V} + [\hat{S}, \hat{H}_0] = 0$. We use the ansatz $\hat{S} = \alpha(\hat{J}^- \hat{A} - \hat{A} \hat{J}^+)$, and compute

$$[\hat{S}, \hat{H}_0] = \alpha \Delta [\hat{J}^- \hat{A} - \hat{A} \hat{J}^+, \hat{J}^z] = \alpha \Delta (\hat{J}^- \hat{A} + \hat{A} \hat{J}^+),$$

where we used $[\hat{A}, \hat{J}^z] = 0$ and $[\hat{J}^\pm, \hat{J}^z] = \mp \hat{J}^\pm$. Matching $[\hat{S}, \hat{H}_0] = -\hat{V}$ gives $\alpha = -g/\Delta$, so that

$$\hat{S} = \frac{g}{\Delta} (\hat{A} \hat{J}^+ - \hat{J}^- \hat{A}).$$

The effective dispersive Hamiltonian then becomes

$$\begin{aligned} \hat{H}_{\text{disp}} &\approx \hat{H}_0 + \frac{1}{2} [\hat{S}, \hat{V}] \\ &= \Delta \hat{J}^z + \frac{g^2}{\Delta} [2(n_{\text{ex}} - N/2) \hat{J}^z + 2(\hat{J}^z)^2 - \hat{J}^- \hat{J}^+] \\ &= \left(\Delta + \frac{2g^2}{\Delta} (n_{\text{ex}} - N/2) \right) \hat{J}^z + \frac{2g^2}{\Delta} (\hat{J}^z)^2 - \frac{g^2}{\Delta} \hat{J}^- \hat{J}^+, \end{aligned} \quad (\text{B4})$$

which equals Eq. (3), and is similar to previous derivations [42, 43]. Analyzing this approximated Hamiltonian From Eq. (B4), although not exact, can give a good understanding of the possible gates, and show how the combination of n_{ex} , the ratio g^2/Δ^2 , and the gate duration, determine the executed gate.

3. The controlled-parity gate

To reach the controlled-parity gate, we examine a case where the joint system of the qubits and the battery are in a superposition of two subspaces with n_{ex} and $n_{\text{ex}} - 1$, corresponding to an ancillary qubit in $|0\rangle$ or $|1\rangle$, respectively. Then, a superposition of dispersive gate will be applied, $U_{\text{disp}}(n_{\text{ex}})$ and $U_{\text{disp}}(n_{\text{ex}} - 1)$, where U_{disp} corresponds to evolving the system with Eq. (B4) for $t_{\text{disp}} = \pi/(2g^2/\Delta)$. This is equivalent to a controlled gate in the form of $U_{\text{disp}}(n_{\text{ex}})^{-1} U_{\text{disp}}(n_{\text{ex}} - 1)$.

Eq. (B4) conserves the \hat{J}^z value, which is equivalent to the conservation of the number of qubit excitation, $[Z^{\otimes N}, U_{\text{disp}}] = 0$ for any N . Specifically, Substituting Eq. (B4), shows

$$U_{\text{ent}}(n_{\text{ex}})^{-1} U_{\text{ent}}(n_{\text{ex}} - 1) = e^{2itg^2/\Delta \hat{J}^z}, \quad (\text{B5})$$

as n_{ex} appears in the dispersive Hamiltonian only as the amplitude of the \hat{J}^z operator. Thus, when including the ancillary qubit, the overall unitary matches (up to a global phase) to the desired controlled- $Z^{\otimes N}$ when $t = \pi/(2g^2/\Delta)$, giving

$$U_{\text{ent}}(n_{\text{ex}})^{-1} U_{\text{ent}}(n_{\text{ex}} - 1) = e^{i\hat{J}^z \pi} = (-1)^{\hat{J}^z} = i^N Z^{\otimes N},$$

enabling probing any $Z^{\otimes N}$ operator with a single dispersive gate, regardless of the initial cavity state. Including local gates can extend this probing to $X^{\otimes N}$, completing the required stabilizers for QEC codes.

Appendix C: Reaching Universal Gate Set in Quantum Battery Computation

As discussed above, the system may implement entangling gates and can perform Z rotations of arbitrary angles by detuning a single qubit relative to the others. According to the the Solovay-Kitaev theorem [60], completing a universal gate set hinges upon the ability to implement a local, non-trivial energy-changing gate: modifying the population of one qubit (non-trivially) without affecting the states of the remaining qubits, and regardless of the system's state.

To see how this is reached in a two-qubit system with a QB, we can set one qubit to zero detuning ($\Delta_0 = 0$) and the other highly detuned ($\Delta_1 \gg g$), ensuring that the highly detuned qubit experiences only a phase shift without changing its population. In this configuration, the subsystem of qubit 0 and the battery shares either n_{ex} quanta when qubit 1 is in $|0\rangle$ or $n_{\text{ex}} - 1$ quanta when qubit 1 is in $|1\rangle$, with corresponding Rabi frequencies $2g\sqrt{n_{\text{ex}}}$ and $2g\sqrt{n_{\text{ex}} - 1}$. The same gate operation in both cases occurs when the condition $\Omega_n t = \Omega_{n-1} t + 2\pi j$ is satisfied, where j is a non-zero integer. Choosing a gate duration

$$t = \frac{\pi}{g(\sqrt{n_{\text{ex}}} - \sqrt{n_{\text{ex}} - 1})}$$

for $j = 1$ executes on qubit 0 the gate X^α with

$$\alpha = \frac{\sqrt{n_{\text{ex}} - 1}}{\sqrt{n_{\text{ex}}} - \sqrt{n_{\text{ex}} - 1}},$$

independently on the state of qubit 1. The non-trivial α ensures that the gate completes the universal gate set.

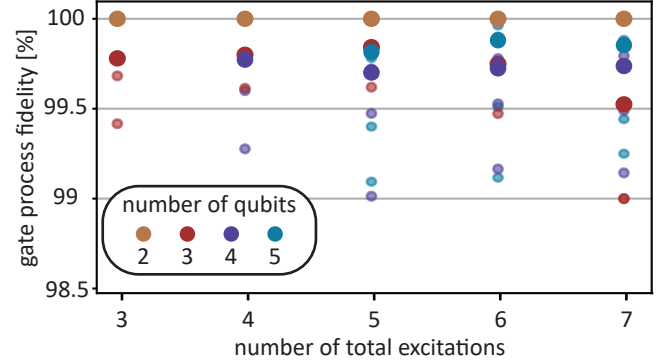


FIG. 7. Fidelity of the non-Pauli energy-exchange gate as a function of the total number of photons in the battery for different multi-qubit systems. The shaded circles represent the fidelities between all possible unitary gates that can be implemented, depending on the initial state of the joint battery-qubit system. For systems with three or more qubits, the average gate fidelity remains above 99.5%, while the worst-case fidelity exceeds 99%, when using a two-step detuning process. In the two-qubit case, a single detuning step achieves 100% fidelity.

This logic extends to larger systems, but without a guarantee of implementing the exactly same single-qubit gate independently on the other qubits' state. To fill this gap, we exploit additional degrees of freedom: the detuning Δ_0 , the number of discrete steps (i.e., changing detunings over time), and their duration. For example, in a three-qubit system with a quantum battery initialized to $n_{\text{ex}} = 5$, applying detunings of $6.5g$ and $-6.76g$ to one qubit for durations of 24.13 and 24.54 (in units of $1/g$) implements a 0.96π rotation around the axis $(0.07, 0.811, 1)$ with 100% fidelity when the other two qubits are in the $\{|01\rangle, |10\rangle\}$ subspace. If the other two qubits are in $|00\rangle$ or $|11\rangle$, the process fidelities (evaluated through $F(U_1, U_2) = \frac{1}{4} |\text{Tr}(U_1^\dagger U_2)|^2$ relative to the $\{|01\rangle, |10\rangle\}$ subspace) are 99.2% and 98.9%, respectively, giving an average fidelity of 99.5%.

We performed numerical optimization of such two-step detuning values and durations for implementing local unitary operations in systems of 3, 4, and 5 qubits with n_{ex} up to 7 excitations. As shown in Fig. 7, worst-case fidelities exceed 99%, and average fidelities surpass 99.5%. This procedure generalizes to systems with arbitrary numbers of qubits, and with more than two steps, enabling local non-trivial energy-changing gates—and thereby completing a universal gate set.

Appendix D: Heat Dissipation Analysis

The goal of this chapter is to compare the conventional quantum computation to the computation powered by QBs, in terms of the created heating power in the bottom two stages of the cryogenic fridge, based on the analysis from Ref. [46]. We concentrate on lowest two layers in the cryogenic fridge (cold plate, CP, and mixing chamber, MXC) because they are the hardest to cool, and considered the limiting stages on qubit count. We estimate the qubit count when comparing the generated heat to the cooling power in the state-of-the-art cryogenic system (Bluefors XLD1000sl).

1. Quantum Computation Channel Types

The configuration described here is oriented toward flux-tunable superconducting qubits, though similar analysis applies to fixed-frequency qubits and semiconductor spin qubits. There are five types of channels used: **Drive channels** control XY gates with GHz analog modulated pulses sent through coaxial lines capacitively coupled to the qubit; each qubit has a unique drive channel, and these channels include large attenuation (20 dB at both MXC and CP), generating significant heat without prospects for reduction. Our QB approach removes these channels. **Flux channels** carry currents to set qubit frequencies, requiring stable DC or up to 1–2 GHz signals; with superconducting wiring and mini-

mal attenuation, they contribute negligible heat. **Readout resonator feed channels** apply microwave signals to resonators coupled to qubits, with attenuation like drive drive lines but lower signal amplitudes, resulting in similar passive but less active heat. **Readout output channels** use superconducting cables without attenuators, contributing negligible heat. **Readout amplifier pump channels** drive cryogenic amplifiers (e.g., TW-PAs) with ~ -55 dBm signal in the MXC; these lines have 10 dB less attenuation in CP than drive lines but require significantly more power, making their active load comparable to drive channels.

We consider three cable options: **Stainless steel coaxial cables** (UT-085-SS-SS) for channels with attenuators; **Niobium-titanium cables** (UT-085-NbTi) for channels without attenuators, we use passive loads from theoretical calculations and assume negligible active loads when superconducting; and **Optimal superconducting cables**, analyzed as twisted-pair wires with passive loads estimated from Ref. [46].

In this derivation, we compare the heat generated during quantum computation among the standard architecture, the QB architecture with standard cables, and the QB architecture with superconducting cables. Table I summarizes the cable configurations for these three architectures.

Architecture	Drive	Flux	feed	Output	Pump
Standard	SS	SS	SS	NbTi	SS
QB	SS	SS	SS	NbTi	SS
Standard w. SC cables	SS	opt	SS	NbTi	SS
QB w. SC cables	SS	opt	SS	NbTi	SS

TABLE I. Cable configuration for the analyzed architectures. The cable types are: stainless steel coaxial cables (SS), niobium-titanium cables (NbTi), and optimal superconducting cables (opt).

2. Analysis of the generated heat

There are two fundamentally different sources of heat: passive load and active load.

Passive loads corresponds to heat generated by thermal fluctuations at room temperature conducted down through cables with non-zero thermal conductivity. Passive heat is produced along the cables due to their thermal resistivity and within attenuators. In this analysis, we use the calculated passive heat per cable shown in Table II. Data is based on Table 2 from Ref. [46], considering the authors note that measured values might overestimate the exact passive heat. Passive heat from drive and flux lines differ due to different attenuator configurations. Optimal superconducting wire passive heat is taken from twisted-pair data in Fig. 1 of Ref. [46].

The total expected passive heat per qubit in each configuration is shown in Table III. We use the cable configuration from Table I in addition to the expected multiplex-

ing in readout line and the passive heat from the attenuators. For the QB configurations, we keep one drive line per 10 qubits to account for the lines required for charging the cavity. This additional line adds only passive heat as the battery is charged prior to the computation.

Cable type	CP passive load	MXC passive load
UT-085-SS-SS (Drive)	365 nW	8.5 nW
UT-085-SS-SS (Flux)	270 nW	17 nW
UT-085-NbTi (NbTi)	240 nW	11 nW
Optimal SC wire (opt)	1 nW	0.01 nW

TABLE II. Calculated passive heat per cable type at CP and MXC stages. Values from Table 2 in Ref. [46], averaged between measured and estimated passive heat. Optimal wire parameters are from Fig. 1 in Ref. [46].

Architecture	CP passive	MXC passive
Standard	$P_{p,CP} = 756$ nW	$P_{p,MXC} = 29$ nW
QB	$P_{p,CP} = 427$ nW	$P_{p,MXC} = 21.35$ nW
Standard w. SC cables	$P_{p,CP} = 487$ nW	$P_{p,MXC} = 12$ nW
QB w. SC cables	$P_{p,CP} = 158$ nW	$P_{p,MXC} = 4.36$ nW

TABLE III. total passive heat per qubit for each option, given the cable configuration above. The standard case is calculated through 1.25 SS drive cables, 1 SS flux, and 0.125 NbTi cables per qubit. The QB case is calculated through 0.35 SS drive cables, 1 SS flux, and 0.125 NbTi. The standard with SC cables case is calculated through 1.25 SS drive cables, 1 opt cable and 0.125 NbTi cables per qubit. The QB with SC cables case is calculated through 0.35 SS drive cables, 1 opt cable and 0.125 NbTi cables per qubit.

Active loads arise from the external (electromagnetic) control pulses which dissipates along its path inside the cryogenic fridge, either within the cables or within attenuators. Attenuation is mandatory to reduce the incoming noise radiation field. That is, attenuators are needed to block the high occupation of room-temperature photons to reach the quantum computer and modify the quantum state. As a result, the input powers of the drive signals in room temperature are significantly larger than what are used to interact with the qubits. The active heat for each channel is:

Drive channels – Include 60 dB total attenuation (10^6 photon suppression), with 20 dB each at the MXC and CP. Ref.[46] estimates average power per 20 ns π -pulse as $P_{avg}(\pi) \approx -71$ dBm (8×10^{-11} W), and per $\pi/2$ pulse as $P_{avg}(\pi/2) \approx -77$ dBm. Accounting for an average duty cycle of $D = 0.2$ per qubit (surface-code QEC + dynamical decoupling), the average active power per qubit becomes $P_{avg} = D(P_{avg}(\pi) + P_{avg}(\pi/2))$, giving:

$$P_{a,MXC}^D = 10^2 P_{avg} = 2.5 \text{ nW}, \quad P_{a,CP}^D = 10^4 P_{avg} = 250 \text{ nW}.$$

In the QB configurations, drive lines used for battery charging do not create active heat since charging is performed before computation.

Flux channels – Dissipation arises mainly from DC bias currents setting qubit frequencies. Ref.[46] gives

worst-case estimates of $0.050 \mu\text{W}$ (MXC) and $0.140 \mu\text{W}$ (CP) per channel. Including $\sim 1/6$ additional overhead for entangling gates but reducing by a factor of 3 (with some magnetic shielding) gives:

$$P_{a,MXC}^F = 20 \text{ nW}, \quad P_{a,CP}^F = 54 \text{ nW}.$$

In the optimal SC cable case, flux active loads are negligible.

Readout resonator feed lines – Signals are $\sim 10 \times$ smaller than qubit drive channels. Assuming the same duty cycle but with one channel per 8 qubits gives per-qubit powers:

$$P_{a,MXC}^{RD} = 30 \text{ pW}, \quad P_{a,CP}^{RD} = 3 \text{ nW}.$$

Readout output channels – Do not contribute active heat. **Readout amplifier pump channels** – Pumping an amplifier requires ~ -60 dBm input with 10% duty cycle, attenuated by 50 dB total (10 dB in CP, 20 dB in MXC). With one pump per 8 qubits:

$$P_{a,MXC}^P = 2.5 \text{ nW}, \quad P_{a,CP}^P = 25 \text{ nW}.$$

Table IV summarizes the sum of both active and passive heat per qubit per configuration for each cryogenic stage. The total number of qubits per fridge is derived by taking these heating powers and comparing them to the state-of-the-art cryogenic fridge (Bluefors XLD1000sl) cooling powers of $P_{cool,MXC} = 34 \mu\text{W}$ and $P_{cool,CP} = 1000 \mu\text{W}$. When taking the minimum in the number of potential qubits in the CP and the MXC we find the overall qubit limit of the cryogenic fridge per configuration, shown in Table V. In Fig. 8 we show the contribution of the different heat sources in the overall cooling budget. We note that as opposed to the results in [46], the limit comes from the MXC and not the CP stage, since the current state-of-the-art cryogenic fridge has improved the CP cooling power by a factor of 5 while the MXC cooling power was improved by a factor of 1.7.

Architecture	CP total	MXC total
Standard	1024 nW	52 nW
QB	497 nW	42 nW
Standard w. SC cables	701 nW	15.2 nW
QB w. SC cables	173 nW	5.6 nW

TABLE IV. Total heat per qubit per configuration, combining passive and active loads.

Architecture	CP qubits	MXC qubits	Limit
Standard	976	657	657
QB	2011	808	808
Standard w. SC cables	1426	2226	1426
QB w. SC cables	5755	6033	5755

TABLE V. Estimated maximum number of qubits per configuration, derived from total heat per qubit and fridge cooling capacities.

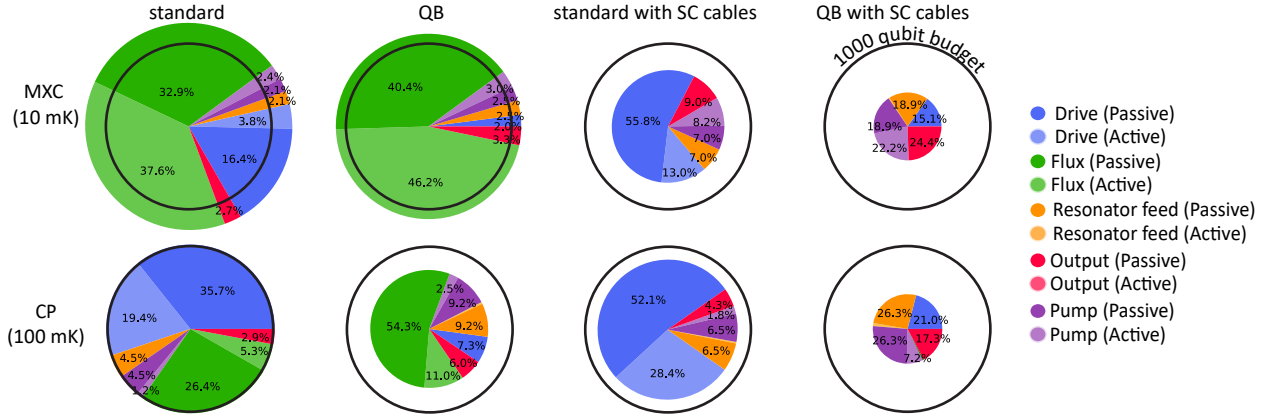


FIG. 8. Heat power source distribution for the examined computation architecture.

3. Computation Energy Analysis

Power calculations shown in Fig. 6c are based on active heat dissipation at the CP, scaled by total attenuation up to room temperature. For a cycle duration of $1\mu\text{s}$, each gate contributes power according to the duty cycles described earlier. The flux channels add 10 dB, pump channels add 20 dB, and drive/readout drive channels add 20 dB relative to CP power levels. For QB implementations, we add an energy overhead equivalent to 100 rounds of average drive power for a single qubit.

Appendix E: Circuit simulation details

All quantum simulations were performed in Python using the QuTiP package. For the superextensive compu-

tation shown in Fig. 3 of the main text, we employed an extended Hilbert space that includes both cavity and qubit degrees of freedom. In contrast, all other simulations used a reduced Hilbert space of dimension 2^N , corresponding to the cavity–qubit dressed states. In Fig. 3, all qubits were set to zero detuning, and the gate duration was chosen as the time maximizing fidelity with the target state $|1\rangle^{\otimes N}$. For Fig. 4, detuning values and durations were optimized for each gate in the circuit using SciPy’s minimize function, with the cost function defined as the Hilbert–Schmidt distance between the implemented and target unitaries. In the simulations of Fig. 5, detuning values and gate durations were optimized to maximize the fidelity to the intermediate states in Fig. 5c, and to the final state in Fig. 5d. In these cases (and in Fig. 4), we allowed optimization across multiple gate steps. We found that providing initial guesses informed by analytical approximations significantly improved convergence speed of the numerical optimization.

[1] R. Alicki and M. Fannes, Entanglement boost for extractable work from ensembles of quantum batteries, *Physical Review E—Statistical, Nonlinear, and Soft Matter Physics* **87**, 042123 (2013).

[2] F. Campaioli, S. Gherardini, J. Q. Quach, M. Polini, and G. M. Andolina, Colloquium: quantum batteries, *Reviews of Modern Physics* **96**, 031001 (2024).

[3] F. Campaioli, F. A. Pollock, F. C. Binder, L. Céleri, J. Goold, S. Vinjanampathy, and K. Modi, Enhancing the charging power of quantum batteries, *Physical review letters* **118**, 150601 (2017).

[4] D. Ferraro, M. Campisi, G. M. Andolina, V. Pellegrini, and M. Polini, High-power collective charging of a solid-state quantum battery, *Physical review letters* **120**, 117702 (2018).

[5] S. Julià-Farré, T. Salamon, A. Riera, M. N. Bera, and M. Lewenstein, Bounds on the capacity and power of quantum batteries, *Physical Review Research* **2**, 023113 (2020).

[6] J. Q. Quach, G. Cerullo, and T. Virgili, Quantum batteries: The future of energy storage?, *Joule* **7**, 2195 (2023).

[7] G. M. Andolina, M. Keck, A. Mari, M. Campisi, V. Giovannetti, and M. Polini, Extractable work, the role of correlations, and asymptotic freedom in quantum batteries, *Physical review letters* **122**, 047702 (2019).

[8] R. Grazi, D. Sacco Shaikh, M. Sassetto, N. Traverso Ziani, and D. Ferraro, Controlling energy storage crossing quantum phase transitions in an integrable spin quantum battery, *Physical Review Letters* **133**, 197001 (2024).

[9] T. P. Le, J. Levinsen, K. Modi, M. M. Parish, and F. A. Pollock, Spin-chain model of a many-body quantum battery, *Physical Review A* **97**, 022106 (2018).

[10] D. Rossini, G. M. Andolina, D. Rosa, M. Carrega, and M. Polini, Quantum advantage in the charging process of sachdev-ye-kitaev batteries, *Physical Review Letters* **125**, 236402 (2020).

[11] L. Razzoli, G. Gemme, I. Khomchenko, M. Sassetto, H. Ouerdane, D. Ferraro, and G. Benenti, Cyclic solid-state quantum battery: Thermodynamic characteriza-

tion and quantum hardware simulation, *Quantum Science and Technology* **10**, 015064 (2025).

[12] B. Ahmadi, P. Mazurek, P. Horodecki, and S. Barzanjeh, Nonreciprocal quantum batteries, *Physical Review Letters* **132**, 210402 (2024).

[13] R. H. Dicke, Coherence in spontaneous radiation processes, *Physical review* **93**, 99 (1954).

[14] J. Q. Quach, K. E. McGhee, L. Ganzer, D. M. Rouse, B. W. Lovett, E. M. Gauger, J. Keeling, G. Cerullo, D. G. Lidzey, and T. Virgili, Superabsorption in an organic microcavity: Toward a quantum battery, *Science advances* **8**, eabk3160 (2022).

[15] K. Hymas, J. B. Muir, D. Tibben, J. van Embden, T. Hirai, C. J. Dunn, D. E. Gómez, J. A. Hutchison, T. A. Smith, and J. Q. Quach, Experimental demonstration of a scalable room-temperature quantum battery, *arXiv preprint arXiv:2501.16541* (2025).

[16] C.-K. Hu, J. Qiu, P. J. Souza, J. Yuan, Y. Zhou, L. Zhang, J. Chu, X. Pan, L. Hu, J. Li, *et al.*, Optimal charging of a superconducting quantum battery, *Quantum Science and Technology* **7**, 045018 (2022).

[17] G. Gemme, M. Grossi, D. Ferraro, S. Vallecorsa, and M. Sassetto, Ibm quantum platforms: A quantum battery perspective, *Batteries* **8**, 43 (2022).

[18] F.-Q. Dou and F.-M. Yang, Superconducting transmon qubit-resonator quantum battery, *Physical Review A* **107**, 023725 (2023).

[19] J. Joshi and T. Mahesh, Experimental investigation of a quantum battery using star-topology nmr spin systems, *Physical Review A* **106**, 042601 (2022).

[20] N. Friis and M. Huber, Precision and work fluctuations in gaussian battery charging, *Quantum* **2**, 61 (2018).

[21] R. R. Rodriguez, B. Ahmadi, P. Mazurek, S. Barzanjeh, R. Alicki, and P. Horodecki, Catalysis in charging quantum batteries, *Physical Review A* **107**, 042419 (2023).

[22] G. Chiribella, Y. Yang, and R. Renner, Fundamental energy requirement of reversible quantum operations, *Physical Review X* **11**, 021014 (2021).

[23] A. Auffèves, Quantum technologies need a quantum energy initiative, *PRX Quantum* **3**, 020101 (2022).

[24] C. H. Bennett, Logical reversibility of computation, *IBM journal of Research and Development* **17**, 525 (1973).

[25] S. Vuglar and J. Gea-Banacloche, Recycling of a quantum field and optimal states for single-qubit rotations, *Physical Review A* **109**, 022439 (2024).

[26] M. Tavis and F. W. Cummings, Exact solution for an n-molecule—radiation-field hamiltonian, *Physical Review* **170**, 379 (1968).

[27] J. Q. Quach and W. J. Munro, Using dark states to charge and stabilize open quantum batteries, *Physical Review Applied* **14**, 024092 (2020).

[28] S. Jandura, V. Srivastava, L. Pecorari, G. K. Brennen, and G. Pupillo, Nonlocal multiqubit quantum gates via a driven cavity, *Physical Review A* **110**, 062610 (2024).

[29] M. Renger, J. Verjauw, N. Wurz, A. Hosseinkhani, C. Ockeloen-Korppi, W. Liu, A. Rath, M. J. Thapa, F. Vigneau, E. Wybo, *et al.*, A superconducting qubit-resonator quantum processor with effective all-to-all connectivity, *arXiv preprint arXiv:2503.10903* (2025).

[30] P. Bertet, C. Harmans, and J. Mooij, Parametric coupling for superconducting qubits, *Physical Review B—Condensed Matter and Materials Physics* **73**, 064512 (2006).

[31] J. A. Mlynek, A. A. Abdumalikov, C. Eichler, and A. Wallraff, Observation of dicke superradiance for two artificial atoms in a cavity with high decay rate, *Nature communications* **5**, 5186 (2014).

[32] Z. Wang, H. Li, W. Feng, X. Song, C. Song, W. Liu, Q. Guo, X. Zhang, H. Dong, D. Zheng, *et al.*, Controllable switching between superradiant and subradiant states in a 10-qubit superconducting circuit, *Physical review letters* **124**, 013601 (2020).

[33] H. Wang, M. Hofheinz, M. Ansmann, R. Bialczak, E. Lucero, M. Neeley, A. O’connell, D. Sank, J. Wenner, A. Cleland, *et al.*, Measurement of the decay of fock states in a superconducting quantum circuit, *Physical Review Letters* **101**, 240401 (2008).

[34] X. Deng, S. Li, Z.-J. Chen, Z. Ni, Y. Cai, J. Mai, L. Zhang, P. Zheng, H. Yu, C.-L. Zou, *et al.*, Quantum-enhanced metrology with large fock states, *Nature Physics*, 1 (2024).

[35] J. Gea-Banacloche and M. Ozawa, Minimum-energy pulses for quantum logic cannot be shared, *Physical Review A—Atomic, Molecular, and Optical Physics* **74**, 060301 (2006).

[36] K. Mølmer and A. Sørensen, Multiparticle entanglement of hot trapped ions, *Phys. Rev. Lett.* **82**, 1835–1838 (1999).

[37] C. Song and *et al.*, 10-qubit entanglement and parallel logic operations with a superconducting circuit, *Phys. Rev. Lett.* **119**, 180511 (2017).

[38] S. M. Young, N. T. Jacobson, and J. R. Petta, Optimal control of a cavity-mediated iswap gate between silicon spin qubits, *Phys. Rev. Appl.* **18**, 064082 (2022).

[39] J. Dijkema, X. Xue, P. Harvey-Collard, M. Rimbach-Russ, S. L. de Snoo, G. Zheng, A. Sammak, G. Scappucci, and L. M. Vandersypen, Cavity-mediated iswap oscillations between distant spins, *Nature Physics* **21**, 168 (2025).

[40] M. A. Nielsen and I. L. Chuang, *Quantum Computation and Quantum Information* (Cambridge University Press, 2012).

[41] C. Song and *et al.*, Generation of multicomponent atomic schrödinger cat states of up to 20 qubits, *Science* **365**, 574–577 (2019).

[42] S.-B. Zheng, One-step synthesis of multiatom greenberger-horne-zeilinger states, *Physical Review Letters* **87**, 230404 (2001).

[43] G. Gemme, G. M. Andolina, F. M. D. Pellegrino, M. Sassetto, and D. Ferraro, Off-resonant dicke quantum battery: Charging by virtual photons, *Batteries* **9**, 197 (2023).

[44] A. Sørensen and K. Mølmer, Quantum computation with ions in thermal motion, *Physical review letters* **82**, 1971 (1999).

[45] C. D. Bruzewicz, J. Chiaverini, R. McConnell, and J. M. Sage, Trapped-ion quantum computing: Progress and challenges, *Applied physics reviews* **6** (2019).

[46] S. Krinner, S. Storz, P. Kurpiers, P. Magnard, J. Heinssoo, R. Keller, J. Luetolf, C. Eichler, and A. Wallraff, Engineering cryogenic setups for 100-qubit scale superconducting circuit systems, *EPJ Quantum Technology* **6**, 2 (2019).

[47] S. S. Pratapsi, L. Buffoni, and S. Gherardini, Competition of decoherence and quantum speed limits for quantum-gate fidelity in the jaynes-cummings model, *Physical Review Research* **6**, 023296 (2024).

[48] F. Lecocq, F. Quinlan, K. Cicak, J. Aumentado, S. Did-dams, and J. Teufel, Control and readout of a superconducting qubit using a photonic link, *Nature* **591**, 575 (2021).

[49] M. Hofheinz, E. Weig, M. Ansmann, R. C. Bialczak, E. Lucero, M. Neeley, A. O'connell, H. Wang, J. M. Martinis, and A. Cleland, Generation of fock states in a superconducting quantum circuit, *Nature* **454**, 310 (2008).

[50] N. Rivera, J. Sloan, I. Kaminer, and M. Soljačić, Nonperturbative electromagnetic nonlinearities, n-photon reflectors, and fock-state lasers based on deep-strong coupling of light and matter, *Physical Review Research* **5**, 043240 (2023).

[51] M. A. Rol, L. Ciorciaro, F. K. Malinowski, B. M. Tarasinski, R. E. Sagastizabal, C. C. Bultink, Y. Salathe, N. Haandbæk, J. Sedivy, and L. DiCarlo, Time-domain characterization and correction of on-chip distortion of control pulses in a quantum processor, *Applied Physics Letters* **116** (2020).

[52] T. Orell, M. Zanner, M. L. Juan, A. Sharafiev, R. Albert, S. Oleshko, G. Kirchmair, and M. Silveri, Collective bosonic effects in an array of transmon devices, *Physical Review A* **105**, 063701 (2022).

[53] J. Majer, J. Chow, J. Gambetta, J. Koch, B. Johnson, J. Schreier, L. Frunzio, D. Schuster, A. A. Houck, A. Wallraff, *et al.*, Coupling superconducting qubits via a cavity bus, *Nature* **449**, 443 (2007).

[54] P. Zhao, K. Linghu, Z. Li, P. Xu, R. Wang, G. Xue, Y. Jin, and H. Yu, Quantum crosstalk analysis for simultaneous gate operations on superconducting qubits, *PRX quantum* **3**, 020301 (2022).

[55] S. Pauka, K. Das, R. Kalra, A. Moini, Y. Yang, M. Trainer, A. Bousquet, C. Cantaloube, N. Dick, G. Gardner, *et al.*, A cryogenic cmos chip for generating control signals for multiple qubits, *Nature Electronics* **4**, 64 (2021).

[56] P. J. Liebermann and F. K. Wilhelm, Optimal qubit control using single-flux quantum pulses, *Physical Review Applied* **6**, 024022 (2016).

[57] A. Opremcak, C. Liu, C. Wilen, K. Okubo, B. Christensen, D. Sank, T. White, A. Vainsencher, M. Giustina, A. Megrant, *et al.*, High-fidelity measurement of a superconducting qubit using an on-chip microwave photon counter, *Physical Review X* **11**, 011027 (2021).

[58] Yaniv Kurman, Dataset associated with 'Powering Quantum Computation with Quantum Batteries', <https://doi.org/10.6084/m9.figshare.29442464.v1> (2025), accessed: 2025-07-01.

[59] R. Shankar, *Principles of quantum mechanics* (Springer Science & Business Media, 2012).

[60] C. M. Dawson and M. A. Nielsen, The solovay-kitaev algorithm, *arXiv preprint quant-ph/0505030* (2005).